Active engineering of four-wave mixing spectral correlations in multiband hollow-core fibers

Martin Cordier, Adeline Orieux, Benoît Debord, Frédéric Gérôme, A. Gorse, Matthieu Chafer, Eleni Diamanti, Philippe Delaye, Fetah Benabid, Isabelle Zaquine

HAL Id: hal-02141395

https://hal.sorbonne-universite.fr/hal-02141395

Submitted on 27 May 2019

Active engineering of four-wave mixing spectral correlations in multiband hollow-core fibers

M. CORDIER,[1] A. ORIEUX,[2] B. DEBORD,[3,4] F. GÉROME,[3,4] A. GORSE,[4] M. CHAFER,[3,4] E. DIAMANTI,[2] P. DELAYE,[5] F. BENABID,[3,4] AND I. ZAQUINE[1,*]

[1] *Laboratoire de Traitement et Communication de l'Information, Télécom ParisTech, Université Paris-Saclay, 75013 Paris, France*
[2] *Laboratoire d'Informatique de Paris 6, CNRS, Sorbonne Université, 75005 Paris, France*
[3] *GPPMM Group, XLIM Research Institute, CNRS UMR 7252, Université de Limoges, Limoges, France*
[4] *GLOphotonics S.A.S., 123 avenue Albert Thomas, Limoges, France*
[5] *Laboratoire Charles Fabry, Institut d'Optique Graduate School, CNRS, Université Paris-Saclay, 91127 Palaiseau cedex, France*
[*] *isabelle.zaquine@telecom-paristech.fr*

Abstract: We demonstrate theoretically and experimentally a high level of control of the four-wave mixing process in an inert gas–filled inhibited-coupling guiding hollow-core photonic crystal fiber. The specific multiple-branch dispersion profile in such fibers allows both correlated and separable bi-photon states to be produced. By controlling the choice of gas and its pressure and the fiber length, we experimentally generate various joint spectral intensity profiles in a stimulated regime that is transferable to the spontaneous regime. The generated profiles may cover both spectrally separable and correlated bi-photon states and feature frequency tuning over tens of THz, demonstrating a large dynamic control that will be very useful when implemented in the spontaneous regime as a photon pair source.

1. Introduction

Entanglement is a key resource in quantum information and strong effort has been made to increase the Hilbert space dimension of the generated quantum states either through the number of particles involved or through the generation of qudits with dimension $d \gg 2$ [1–5]. However, in some applications, it is required to go against this trend and to look for separable states. This is particularly driven by the requirement to generate pure states, through heralding from multipartite states. One emblematic example is a heralded single photon source based on parametric photon pair generation. The purity of the heralded photon can be obtained only if the entanglement in all degrees of freedom (spatial, polarization, spectral) is removed between the photon and its heralding twin [6,7]. In other terms, the photon-pair state must be engineered into a separable state. While removing spatial and polarization entanglement can be easily achieved, the suppression of spectral correlations is generally challenging. It requires stringent conditions on the optical nonlinear process and more specifically on the phase-matching condition. This is exemplified with bulk crystals, commonly used in photon pair generation, and the limited wavelength range where the required conditions can be satisfied [7]. Integrated sources offer more flexibility in engineering the spectral entanglement at specific wavelengths, for instance by designing the poling period of the waveguide [8] or the microstructuration in photonic crystal fiber [9, 10]. Within this context, tuning the photon pairs phase-matched frequencies has been reported using temperature control of a photonic chip [11], or fiber [12]. Furthermore, promising results have been obtained using modulation instability in gas-filled hollow-core photonic crystal fibers, where the amount of spectral correlations of bright twin beams was controlled through gas pressure, chirp and length tuning [13]. Such a source has the further advantage of being

devoid of Raman scattering noise thanks to the use of noble gas. However, modulation instability requires a strong self-phase modulation in order to generate signal and idler whose spectra are not overlapping with the pump spectrum [14]. We therefore have chosen to use four-wave mixing (FWM) where signal and idler can be well separated from the pump in a low gain regime, making it suited for spectral engineering in the photon pair regime [15].

We propose the first demonstration of spectral correlation engineering through a four-wave mixing involving multiple transmission bands of the fiber. The given medium is a gas-filled inhibited-coupling (IC) guiding hollow-core photonic crystal fiber (HCPCF) with controllable dispersion and optical nonlinearity. We used this feature to generate various joint spectral intensity (JSI) profiles, thus indicating the possibility to produce various degrees of spectral correlations. This is a first experimental step toward a versatile fibered and Raman-free photon-pair source.

2. Spectral entanglement

The bi-photon state produced by spontaneous four-wave mixing (SFWM) in an optical fiber of length L is given below using a standard perturbative approach [16]:

$$|\psi_{pair}\rangle = \kappa \int \int d\omega_s d\omega_i F(\omega_s, \omega_i) \hat{a}_s^\dagger(\omega_s) \hat{b}_i^\dagger(\omega_i) |0, 0\rangle \tag{1}$$

Here the quantity κ is a normalizing constant, $\hat{a}_s^\dagger$ and $\hat{b}_i^\dagger$ are the monochromatic creation operators of the two photons s and i of the photon pair and $F(\omega_s, \omega_i)$ is the joint spectral amplitude function (JSA) describing the spectral properties of the generated photon pair. This function can be approximated as the product of the energy conservation function $\alpha(\omega_s, \omega_i)$ and the phase matching function $\phi(\omega_s, \omega_i)$: $F(\omega_s, \omega_i) \approx \alpha(\omega_s, \omega_i) \phi(\omega_s, \omega_i)$.

In FWM with degenerate pump, the energy conservation function is defined as the autoconvolution of the pump spectral amplitude $\alpha = [A * A](\omega_s + \omega_i)$ with $A(\omega)$ usually described by a Gaussian function of width σ. The phase matching function is given by:

$$\phi = \text{sinc}\left[\Delta k_{\text{lin}}(\omega_s, \omega_i)\frac{L}{2}\right] \times \exp\left[i\Delta k_{\text{lin}}(\omega_s, \omega_i)\frac{L}{2}\right], \tag{2}$$

where Δk_{lin} is a first order Taylor expansion of the wavevector mismatch between the photon pair and the pump photon. It is performed around the perfect phase matched frequencies ω_s^0, ω_i^0 and ω_P^0:

$$\Delta k_{\text{lin}}(\omega_s, \omega_i) = (\omega_s - \omega_s^0).(\beta_{1p} - \beta_{1s}) + (\omega_i - \omega_i^0).(\beta_{1p} - \beta_{1i}),$$

where $\beta_{1\mu} = \frac{dk}{d\omega}\big|_{\omega_\mu^0}$ is the inverse group velocity. The spectral correlations can be displayed graphically by mapping F in the (ω_s, ω_i) space as shown in Fig. 1. The energy conservation function α exhibits spectral anti-correlation (Fig 1, left). The shape of the phase matching function can either compensate or reinforce this anti-correlation, depending on its width $\Delta\phi = 1/(L\sqrt{0.096 \times ((\beta_{1p} - \beta_{1s})^2 + (\beta_{1p} - \beta_{1i})^2)})$ and angle $\theta = -\arctan(\frac{\beta_{1p} - \beta_{1s}}{\beta_{1p} - \beta_{1i}})$.

In fact, the JSA profile, chiefly described by θ, $\Delta\alpha$ and $\Delta\phi$, is a direct signature of how the photon-pair states are correlated, as illustrated in Table 1 where we can distinguish two families. The first one comprises factorable states where the signal and idler photons, being spectrally independent, are in a product state. It has been shown [7] that this state can take the form of three distinctive JSA geometry profiles forming a circle or an ellipse along either the horizontal or the vertical axis, each corresponding to a specific phase relationship between the photon pair and the pump. The second family of states that can be identified by JSA profiles relates to what is commonly referred to as correlated states. In such a scenario signal and idler photons are
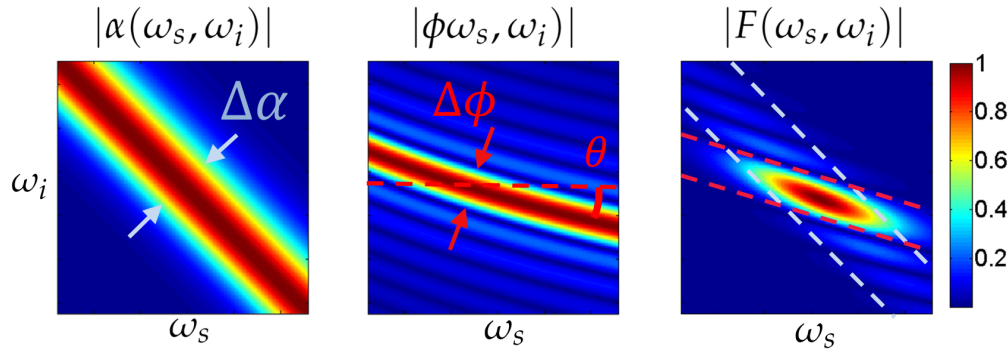
Fig. 1. From left to right: absolute value of the energy conservation function α, the phase matching function ϕ and corresponding joint spectral amplitude in the case of a Gaussian pump in an unengineered medium.

spectrally entangled. A representative JSA of such states is shown on the right hand side panel of Table 1. Here, the JSA typically shows a tilted ellipse profile.

These various degrees of spectral entanglement can be described in a more quantitative way by using the Schmidt decomposition of the JSA, which consists in finding the two sets of orthonormal functions $S_n(\omega_s)$ and $I_n(\omega_i)$ respectively depending only on signal and idler frequency [6]: $F(\omega_s, \omega_i) = \sum_{n=0}^{\infty} \sqrt{c_n} S_n(\omega_s) I_n(\omega_i)$. Substituting into Eq. (1), we obtain:

$$\left| \psi_{pair} \right\rangle = \sum_{n=0}^{\infty} \sqrt{c_n}\, \hat{A}_n^\dagger \, \hat{B}_n^\dagger \left| 0, 0 \right\rangle, \tag{3}$$

where $\hat{A}_n^\dagger = \int d\omega_s S_n(\omega_s) \hat{a}_s^\dagger(\omega_s)$ and $\hat{B}_n^\dagger = \int d\omega_i I_n(\omega_i) \hat{b}_i^\dagger(\omega_i)$ define the temporal modes creation operators. The coefficients c_n are real normalized scalars.
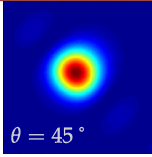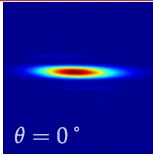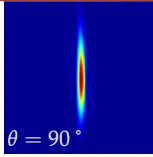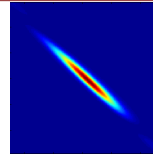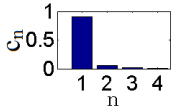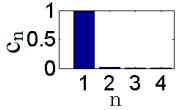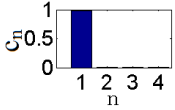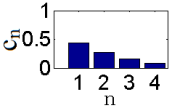
By definition, a factorable state corresponds to the case where there is only one non-zero element in the decomposition so that $\left| \psi_{pair} \right\rangle = \left| A_0 \right\rangle \left| B_0 \right\rangle$ implies spectral independence between signal and idler photons. We also define the mean number of excited modes by the Schmidt number : $K = \frac{1}{\sum_n c_n^2}$. $K = 1$ for a factorable state and $K > 1$ for a correlated state.

These photon-pair states, being spectrally factorable or entangled, are all useful in quantum technology (QT) applications. For example, correlated states are essential in security of quantum key distribution [17], whilst factorable states are the backbone in heralded single photon sources. Furthermore, the temporal mode basis of the signal and idler presented above can be used as an encoding basis in a high dimension Hilbert space [5]. For example, by controlling the Schmidt decomposition one can address the different qudit states of each photon of the pair and tailor the entanglement between these two qudits. A large range of control parameters is required in order to achieve that in a dynamic way with a given source, and we demonstrate here that hollow-core fibers provide the ideal platform for that purpose.

3. Dispersion and group velocity matching conditions in hollow-core fibers

HCPCFs are an exceptional tool for light and fluid-phase interactions thanks to their ability to micro-confine together light and fluids within small modal areas and over interaction lengths that can reach up to kilometers with extremely low optical losses. Furthermore, with a judicious choice of the gas and HCPCF design, gas-filled HCPCFs have been shown to be excellent and versatile platforms for nonlinear and quantum optics [18, 19], with optical nonlinearity and dispersion that can be highly tailored.

Table 1. **Sets of conditions required to obtain either factorable or correlated pair states. Each set defines i) a relation between the group-velocities of pump, signal and idler photons which in turn determines the angle θ ii) a relation between medium length and pump bandwidth.**

Factorable			Correlated
$2\beta_{1p} = \beta_{1s} + \beta_{1i}$	$\beta_{1p} = \beta_{1s}$	$\beta_{1p} = \beta_{1i}$	$\beta_{1p} < \beta_{1s,i}$
$\Delta\phi = \Delta\alpha$	$\Delta\phi \ll \Delta\alpha$	$\Delta\phi \ll \Delta\alpha$	-
$\theta = 45°$	$\theta = 0°$	$\theta = 90°$	

Among the numerous existing fiber designs, we use Inhibited-Coupling guiding HCPCF whose guidance mechanism relies on a principle akin to bound or quasi-bound state in a continuum [20]. In practice, this is achieved by engineering the fiber microstructure such that the coupling between the cladding mode continuum and the core mode is strongly inhibited. Such fiber are sometimes called ARROW [21] in the literature; we refer the reader to [22] for the detailed differences between IC and ARROW. Figure 2 shows a micrograph of our tubular IC-HCPCF and its transmission and dispersion spectra.

IC-HCPCF intrinsically exhibit several bands in their transmission bandwidth spanning from the deep infrared to the UV (see Fig. 2). The corresponding multiple zero-dispersion wavelengths (ZDW) give rise to a large variety of phase-matching and group velocity relations.

An analytical model was recently given to describe the effective index of a $HE_{m,n}$ mode inside
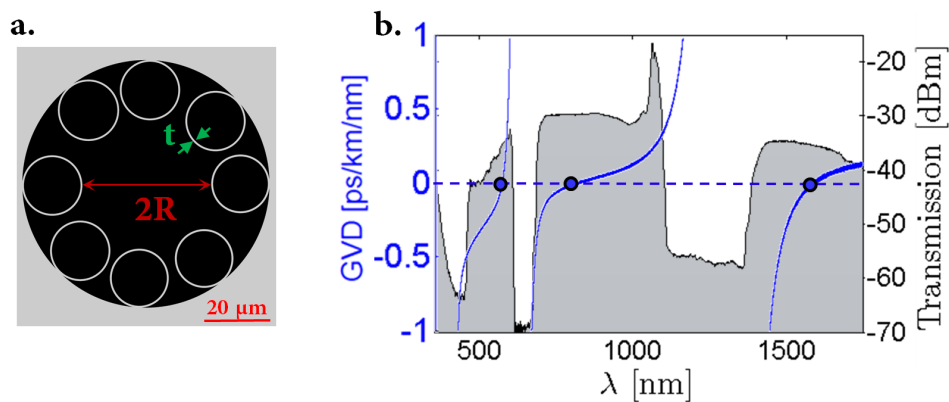
Fig. 2. (a) Fiber cross section (R = 20 μm, $t \approx 630$ nm) and (b) its optical properties. The group-velocity dispersion (blue) is computed with the analytical model whereas the black curve gives the transmitted power for a fiber length of 6.5 m pumped with a super-continuum source. The circles give the position of the zero-dispersion wavelengths. The high peak in the transmission at 1064 nm is a measurement artifact due to the super-continuum pump.

a tube-type hollow core fiber [23]:

$$n_{\text{eff}} = n_{gas} - \frac{j_{m-1,n}^2}{2k_0^2 n_{gas} R^2} - \frac{j_{m-1,n}^2}{k_0^3 n_{gas}^2 R^3} \cdot \frac{\cot\left[\Psi(t)\right]}{\sqrt{\epsilon - 1}} \cdot \frac{\epsilon + 1}{2},$$ (4)

with : $\Psi(t) = k_0 t \sqrt{n_{si}^2 - n_{gas}^2}$, R the fiber radius, $\epsilon = n_{si}^2 / n_{gas}^2$, $j_{m,n}$ the nth root of the mth Bessel function J, t the silica strut thickness and n_{si} the glass refractive index. Simulations and experimental observations have shown that such a tube-type model can provide an accurate description of IC-fiber dispersion [24], provided an effective fiber core radius R_{eff} is used, that is slightly larger than the actual one [25]. Moreover, as long as $\lambda << R$ the evolution of the effective index is, in first approximation, independent of the cladding design around the core. IC fibers can therefore exhibit very close dispersion profiles despite their apparent geometrical difference (i.e tubular lattice, kagome lattice), as long as they have the same radius and silica strut thickness. However, as losses strongly depend on the cladding geometry [26], this simple tube-type model is not suited to infer fiber losses.

The slowly varying contribution of the effective index is described by the first two terms of Eq. (4) depending on gas dispersion and fiber core radius only. The third term introduces the resonances with the silica struts. The positions of these narrow non-guiding regions depend on silica strut thickness t and correspond to $\Psi(t) = l\pi$ with l integer. This defines a set of wavelengths $\lambda_l = \frac{2t}{l}\sqrt{n_{si}^2 - n_{gas}^2}$ where the fiber dispersion is divergent.

Figure 3 shows the dispersion of IC-fibers calculated from Eq. (4) with different silica strut thicknesses t but same radius. For a small t value, the discontinuities λ_l are mostly concentrated in the UV region, such that in the visible and infrared spectral window, the dispersion profile is mainly composed of one transmission band denoted I. As t increases, the discontinuities are red-shifted, forming a more and more multiband dispersion structure (additional bands denoted II, III, ...). The number and position of the bands and ZDWs can therefore be controlled when designing the fiber.

Such multiband dispersion profiles provide an unprecedentedly large control parameter-space in setting the FWM wavelengths (i.e. pump, signal and idler). For example by positioning the three involved wavelengths either in the same band (singleband FWM) or in different bands (multiband FWM), one can control the phase relation between them to span the different bi-photon quantum states mentioned previously. This is illustrated in Fig. 4 where we plot the FWM spectral density map giving both the wavelength of the generated photon and the angle θ of the phase matching as a function of the pump wavelength. The top left hand side corresponds to a simulation neglecting the resonances in the dispersion. In such a case, the phase matching angle θ mainly varies from $-30°$ to $-60°$, thus corresponding to correlated JSA whatever the pump wavelength. In contrast, if the resonances are incorporated in the simulation (Fig. 4 top right hand side), it exhibits a much more diversified phase-matching possibilities. More specifically, new FWM phase matching are available for λ_p in the range [650-750] and [950-1200] nm corresponding to multiband FWM with either signal (M1) or idler (M2) situated in a different dispersion band than the pump (see the bottom insets). In such a multiband configuration, others relations between β_{1p}, β_{1s} and β_{1i} become possible allowing various angles θ. For instance, due to the relative positions of the band between one another (related to the gas pressure), a multiband FWM described by (M1) favours a group velocity matching $\beta_{1p} = \beta_{1i}$ whereas (M2) favours $\beta_{1p} = \beta_{1s}$. Thanks to such multiband FWM, all three factorable states (i.e. $\theta = 0°$, $\theta = 45°$, $\theta = 90°$) become theoretically accessible. To our knowledge, this is the first demonstration that HC-PCF dispersion can be tailored to engineer such a large range of bi-photon quantum states.

The core radius R must also be chosen carefully as it is related to multiple properties, mainly: losses, generation efficiency and modal contents. The FWM generation efficiency varies as R^{-4} which favors a small radius but the general losses also increase with decreasing core radius (R^{-4})
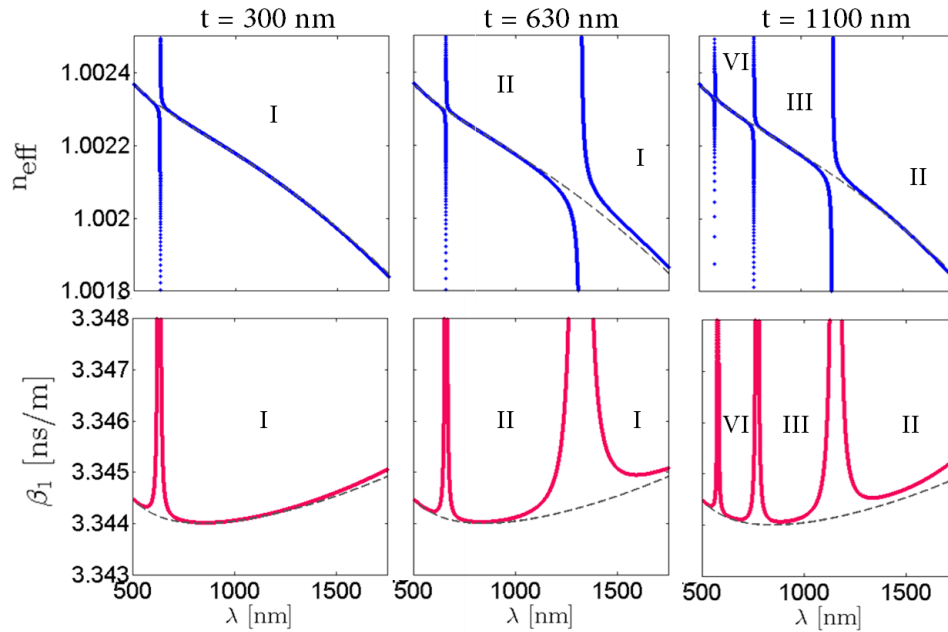
Fig. 3. Top: Effective index and bottom: inverse group velocity β_1 in a IC fiber filled with Xenon (3.5 bar) with a radius of 22 μm for three different silica strut thickness. The Roman numbers to the different bands separated by discontinuities. The gray dashed lines correspond to the dispersion when neglecting the resonances (neglecting last term of Eq. (4)).

which forces a compromise [26]. In such fibers, with a radius around tens of micrometers, the losses are remarkably low ($\approx 10 - 100$ dB/km) at a central wavelength in the band but they increase rapidly as the wavelength approaches a band-edge. None of the involved wavelengths λ_p, λ_s, λ_i should therefore be too close to any discontinuity, which must be taken into account in the fiber design in order to enable efficient FWM. Finally, this type of fiber is usually a few-mode fiber but it can behave as single mode with a careful coupling (Fig. 5(c)).

4. Tomography of the JSI in IC-HCPCF

In order to test our model experimentally we chose a tubular IC-HCPCF composed of 8 tubes with strut thickness $t = 630 \pm 20$ nm. Its 22 ± 1 μm effective core radius offers a good trade-off between losses, generation efficiency and modal content, as explained above. Cross-section and losses are given in Fig. 2 and the simulated phase matching is shown in Fig. 4 right hand side. The fiber design was chosen to exploit a multiband FWM while operating at convenient wavelengths. Indeed, the pump wavelength is set at 1030 nm which is commercially very common. Similarly, the idler wavelength lies at telecom wavelength range, while the signal wavelength is in the range of atomic transitions and Silicon single photon detectors. Nevertheless, using Eq. (4), one can reach any wavelength combination that fulfill energy conservation. Finally the fiber exhibits a polarization extinction ratio of ~ 30 dB.

We use stimulated emission tomography technique (SET) to reconstruct the JSI (= $|JSA|^2$) [27]. Among the existing techniques, SET allows replacing the single photon detectors with fast and spectrally resolved classical detectors provided an additional laser is used at signal or idler wavelength to seed the process. The equivalence of the JSI between spontaneous and stimulated regime is valid only if the variation of the stimulated generated signal power remains linear
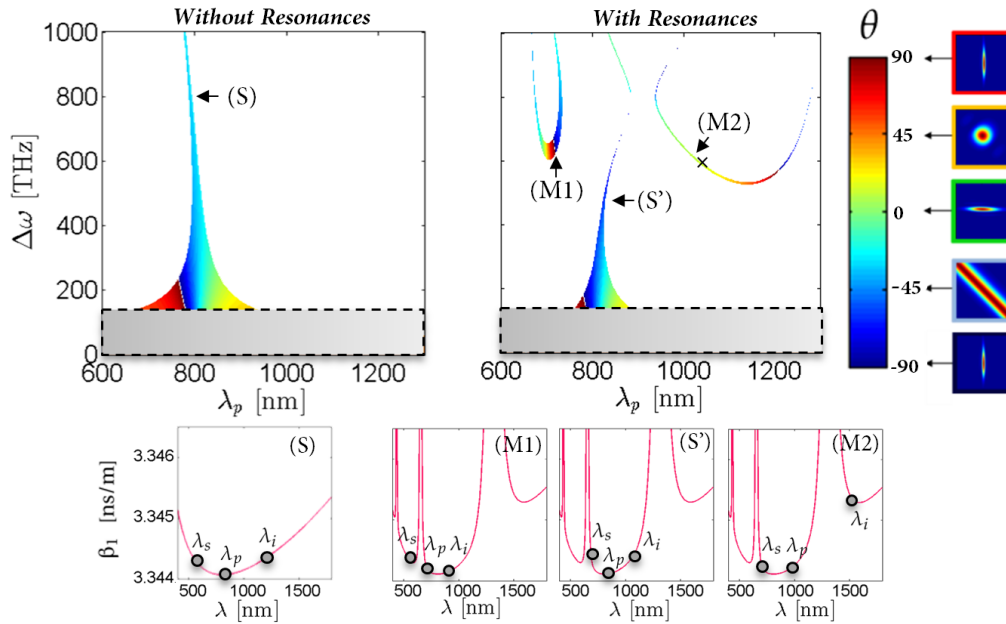
Fig. 4. Top: Simulation comparing the FWM spectral density map with and without neglecting the effect of resonances in the dispersion. The parameters used are the one of our fiber (R = 22 μm, t = 630 nm, and P = 3.5 bar of Xe). The y-axis corresponds to the gap between pump and signal/idler frequencies $\Delta\omega = |\omega_p - \omega_{s/i}|$. The color gives an additional information about the angle θ of the phase matching function. (S) and (S') correspond to a singleband FWM whereas (M1) and (M2) correspond to a multiband FWM. The black cross describes our experimental configuration (λ_p = 1030 nm). The grey region corresponds to FWM where signal and idler are generated too close to the pump wavelength. Note that the lines have been thickened for improved visibility. Bottom: Corresponding group velocity relations.

with seed power [28, 29] (i.e small parametric gain regime). The underlying assumption is that the JSI in the stimulated regime is an amplified version of the JSI in the spontaneous regime; the amplification factor is equal to the average photon number N_{seed} of the coherent seed: $\text{JSI}_{\text{stim}} \approx N_{\text{seed}} \cdot \text{JSI}_{\text{spont}}$.

Our SET experimental characterization setup is shown in Fig. 5. We use a pulsed pump laser (Satsuma, Amplitude Systems) at λ_p = 1030 nm with 280 fs pulse duration at 2 MHz pulse repetition rate and the average pump power injected in the HCPCF is 60 mW. The seed laser (T100, Yenista) is a continuous-wave laser tunable from λ_i = 1530 nm to 1560 nm. The seed power injected in the IC-HC-fiber is around 100 mW, which corresponds to an average power of 50 nW that is effectively involved in the FWM process because of the duty cycle of the pump. Both laser polarizations can be controlled independently with two halfwave plates (HWP). The two fiber ends are inserted into gas-cells with a pressure monitoring and glass windows for optical power injection. Injected into one of the cells, the gas fills the fiber (core and cladding) and an equilibrium between the two gas cells is obtained within less than an hour. At the fiber output, the generated signal at $\omega_s = 2\omega_p - \omega_i$ is filtered with dichroic mirrors and sent to a spectrometer (SILVER-Nova Stellar). For a given seed frequency ω_i, the recorded spectrum gives one horizontal slice of the JSI. The full JSI is composed of all the recorded spectra obtained by sweeping the seed wavelength. The seed power is monitored in order to take into account any power change when tuning ω_i and to normalize the slices. The power dependence of the
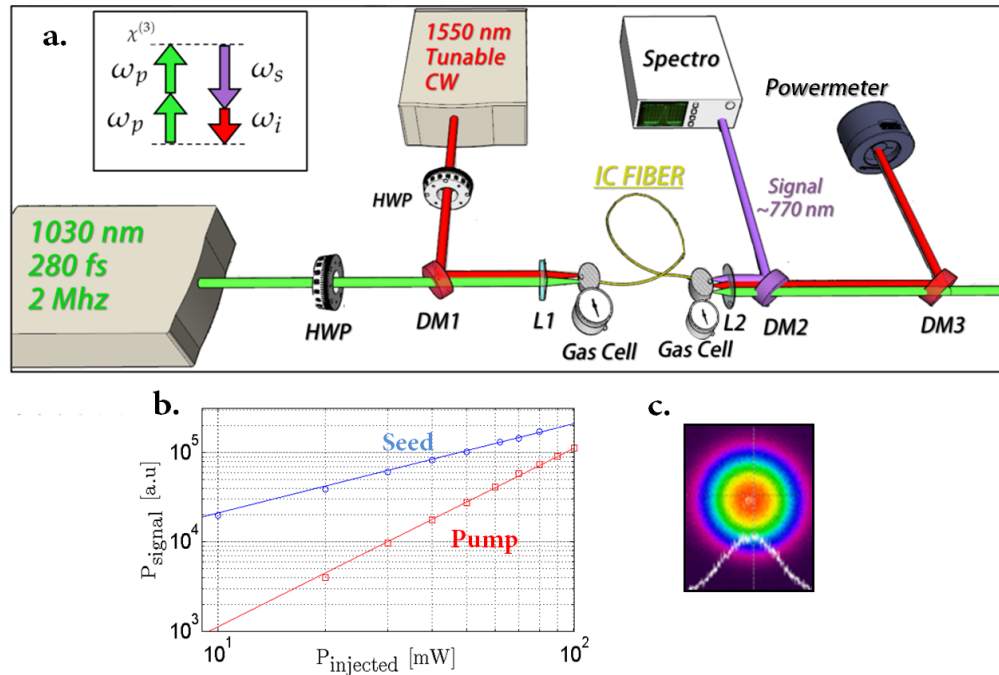
Fig. 5. (a) Experimental setup for the stimulated emission tomography. HWP: half-wave plate, L: lens, DM: Dichroic Mirror. (b) Power generated at the signal frequency as a function of the seed power (blue dots) and of the pump power (red squares), measured at the fiber output. The solid lines correspond to a perfect linear and quadratic dependence (log scale). (c) Measured spatial profile at the fiber output at pump frequency.

power generated at signal frequency as a function of pump power and seed power was measured. Figure 5(b) shows the results confirming the linear dependence versus seed power and quadratic dependence versus pump power, thus validating that our experimental results are transferable to the spontaneous regime [28–30]. Moreover, due to the low nonlinearity, self and cross-phase modulation are here negligible.

Figure 6 illustrates how, by simply changing the fiber length, the bi-photon JSI morphs from the shape of highly correlated states into that of nearly separable states. The figure shows a comparison between experimental and theoretically simulated JSI for fiber lengths going from 40 to 100 cm for the fiber filled with 3.4 bar of xenon as well as the associated Schmidt number K (since simulations assume a flat phase, it is actually a lower bound of K). With a length of 1 meter, the phase matching function and the energy conservation function have about the same width, resulting in an almost factorable state. Decreasing the length implies an increase of the phase matching function width $\Delta\phi$, which gives an increasingly correlated JSI. In the current setup, the minimum fiber length is limited to around 30 cm, mostly due to the size of the two gas cells. The lobe-shaped region in the top right corner of the JSI profile is attributed to the non perfect Gaussian spectral shape of the pump laser pulses. Such shape is due to residual self-phase modulation taking place within the laser and which could be removed using appropriate filters or pulse shaping techniques. The parameters used in the simulation are $t = 630$ nm, $R_{eff} = 22\ \mu$m and $P = 3.4$ bar.
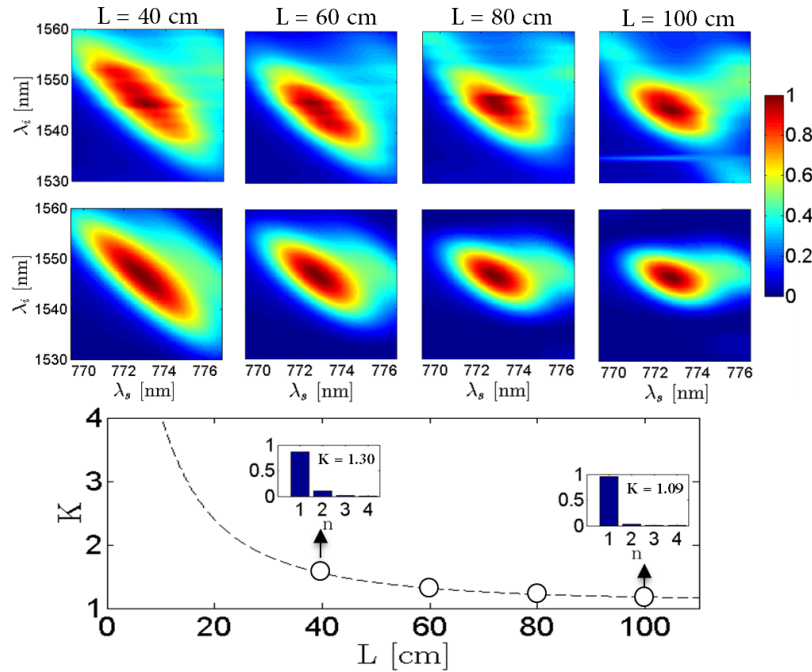
Fig. 6. Top, comparison between experimental (1st row) and simulated (2nd row) JSI for different fiber lengths when filled with 3.4 bar of Xe. The simulation takes into account a modulation in the Gaussian shape of the pump laser spectrum. Bottom, corresponding Schmidt number and Schmidt decomposition (assuming a flat phase).

5. Active tunability of the JSI

An extended control of the spectral properties is possible through the filling gas. Gas temperature and, more notably, pressure can be used to actively impact the dispersion and nonlinear response. The refractive index of the gas at temperature T and pressure P can be extrapolated from the general Sellmeier equation at standard temperature and pressure conditions (T_0, P_0) using:

$$n_{\text{gaz}}(\lambda, P, T) \approx \sqrt{1 + (n_{\text{gaz}}^2(\lambda, P_0, T_0) - 1).\frac{P}{P_0}.\frac{T_0}{T}} \tag{5}$$

The overall dispersion in Eq. (4) results from a competition between the gas dispersion on one side, which is pressure- and temperature-dependent, and the guide dispersion on the other side. Thus, depending on the weight of one relative to the other, the overall dispersion is more or less sensitive to a change of gas refractive index. For instance, fibers with large core have a lower waveguide dispersion. Consequently they will be more sensitive to a change of gas refractive index, caused by a pressure modification. Alternatively, smaller core or fiber filled with light atomic weight gases, will be less sensitive to a change of gas refractive index as the waveguide dispersion will be predominant.

Using the same fiber, we demonstrate this effect by characterizing the JSI of the source as a function of gas pressure, for two different gases, namely argon and xenon (see Fig. 7). Noble gases have been chosen because they are devoid of Raman scattering [31, 32], which eliminates the usual main source of noise in fibered photon-pair generation. The Sellmeier equations of xenon and argon are taken from [33, 34] and their non-linear indices are $n_2 = 9.2 \ 10^{-23}$ and $0.8 \ 10^{-23}$ m^2/W/bar, respectively [35].
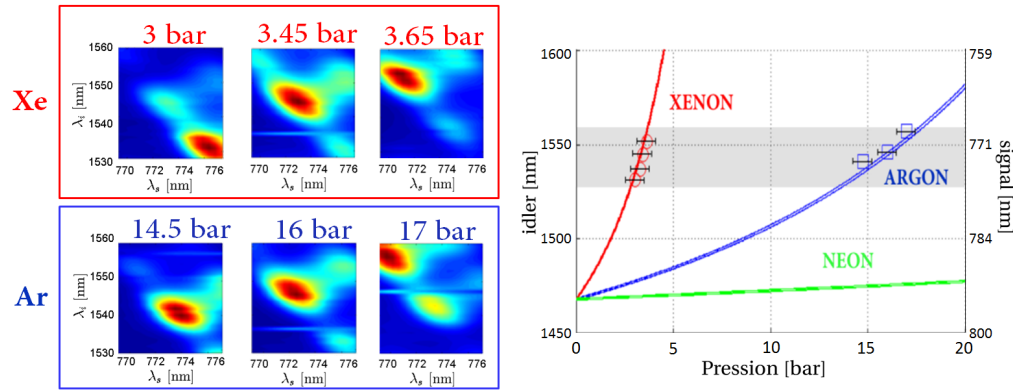
Fig. 7. Left: JSI as a function of gas pressure when filled with xenon and argon Right: Central position of the JSI idler wavelength as a function of gas pressure, for xenon (red circles) and argon (blue squares) and comparison with the simulation. The measurement range in shaded gray was limited by the tunability of the seed laser.

Increasing the pressure has two effects. Firstly, the signal and idler are generated further apart from the pump. For instance, we measured that changing the pressure from 3 bar to 3.65 bar of xenon shifts the idler wavelength from 1531 to 1551 nm and the signal wavelength from 776 to 771 nm. The recorded frequency tuning over $\Delta\omega = 17$ THz is only limited by the tunability of our seed laser. A linearization of the measured data gives a sensitivity of $\Delta\omega = 27.4$ THz/bar in Xe and 5.6 THz/bar in Ar, which can be compared with recent work on temperature tuning in solid core fibers where the reported sensitivity is 0.1 THz/°C [12]. Pressure tuning has the advantages of being compatible with long fibers and free of Raman noise as well as offering both high or low sensitivity according to the gas choice. Secondly, simulation also predicts that changing the pressure slightly rotates the angle θ of the phase matching of $\sim 6°$ per bar of xenon. Adjusting θ can be used, for instance to fine-tune the purity of a heralded single photon source whereas wavelength tuning can be used for instance to aim at a specific telecom channel or atomic transition. With a tunable pump laser, it is also possible to tune the wavelength of one photon while keeping the angle constant and vice-versa.

6. Conclusion

In this paper, we demonstrate that FWM in gas-filled hollow-core fibers provides a versatile platform for generating and manipulating photon-pair states. In particular we show how the intrinsic multiband dispersion of IC fibers can be exploited to access multiband FWM and therefore various JSI shapes corresponding to spectrally factorable or correlated photon pair states. In the case of inhibited-coupling fiber, we present a model relating fiber design, filling medium and dispersion properties to allow for the design of specific fibers for given quantum information applications. It is noteworthy that this very simple model involves only three design parameters, namely fiber core diameter, strut thickness and gas refractive index without adjustable parameter whatsoever.

The experimental results obtained with noble gases validate both the model and the concept of JSI manipulation. A near-factorable JSI is experimentally demonstrated with signal and idler at visible and telecom wavelengths respectively. The effect of fiber length variation on the degree of spectral entanglement as well as the dynamic tuning of the signal and idler wavelength over 17 THz through gas pressure are in perfect agreement with the simulations. Future work will investigate the tailoring of the pump spectral properties with a pulse-shaper for an improved control of the spectral correlations as well as characterizing of the source in the photon pair

regime. Note that, for this off-the-shelf fiber design and a pump of 1 mW, the generation efficiency is expected to be on the order of 10^{-5} pairs/pulse in the spontaneous regime [36]. Furthermore, we believe that using multiband FWM to access tailored spectral correlations can be extended to other media such as for instance sequence of coupled micro-ring resonators [37, 38].

Funding

Acknowledgments

References

1. X.-L. Wang, L.-K. Chen, W. Li, H.-L. Huang, C. Liu, C. Chen, Y.-H. Luo, Z.-E. Su, D. Wu, Z.-D. Li, Y. Hu, X. Jiang, C.-Z. Peng, L. Li, N.-L. Liu, Y.-A. Chen, C.-Y. Lu, and J.-W. Pan, "Experimental ten-photon entanglement," Phys. Rev. Lett. **117**, 210502 (2016).
2. A. Mair, A. Vaziri, G. Weihs, and A. Zeilinger, "Entanglement of the orbital angular momentum states of photons," Nature **412**, 313 (2001).
3. M. Krenn, M. Huber, R. Fickler, R. Lapkiewicz, S. Ramelow, and A. Zeilinger, "Generation and confirmation of a (100× 100)-dimensional entangled quantum system," Proc. Natl. Acad. Sci. U.S.A. **111**, 6243–6247 (2014).
4. M. Malik, M. Erhard, M. Huber, M. Krenn, R. Fickler, and A. Zeilinger, "Multi-photon entanglement in high dimensions," Nat. Photonics **10**, 248 (2016).
5. B. Brecht, D. V. Reddy, C. Silberhorn, and M. Raymer, "Photon temporal modes: a complete framework for quantum information science," Phys. Rev. X **5**, 041017 (2015).
6. C. Law, I. Walmsley, and J. Eberly, "Continuous frequency entanglement: effective finite hilbert space and entropy control," Phys. Rev. Lett. **84**, 5304 (2000).
7. W. P. Grice, A. B. U'Ren, and I. A. Walmsley, "Eliminating frequency and space-time correlations in multiphoton states," Phys. Rev. A **64**, 063815 (2001).
8. A. Eckstein, A. Christ, P. J. Mosley, and C. Silberhorn, "Highly efficient single-pass source of pulsed single-mode twin beams of light," Phys. Rev. Lett. **106**, 013603 (2011).
9. O. Cohen, J. S. Lundeen, B. J. Smith, G. Puentes, P. J. Mosley, and I. A. Walmsley, "Tailored photon-pair generation in optical fibers," Phys. Rev. Lett. **102**, 123603 (2009).
10. C. Söller, B. Brecht, P. J. Mosley, L. Y. Zang, A. Podlipensky, N. Y. Joly, P. S. J. Russell, and C. Silberhorn, "Bridging visible and telecom wavelengths with a single-mode broadband photon pair source," Phys. Rev. A **81**, 031801 (2010).
11. R. Kumar, J. R. Ong, M. Savanier, and S. Mookherjea, "Controlling the spectrum of photons generated on a silicon nanophotonic chip," Nat. Comm. **5**, 5489 (2014).
12. E. Ortiz-Ricardo, C. Bertoni-Ocampo, Z. Ibarra-Borja, R. Ramirez-Alarcon, D. Cruz-Delgado, H. Cruz-Ramirez, K. Garay-Palmett, and A. U'Ren, "Spectral tunability of two-photon states generated by spontaneous four-wave mixing: fibre tapering, temperature variation and longitudinal stress," Quantum Sci. Technol. **2**, 034015 (2017).
13. M. Finger, N. Joly, P. S. J. Russell, and M. Chekhova, "Characterization and shaping of the time-frequency schmidt mode spectrum of bright twin beams generated in gas-filled hollow-core photonic crystal fibers," Phys. Rev. A **95**, 053814 (2017).
14. M. A. Finger, T. S. Iskhakov, N. Y. Joly, M. V. Chekhova, and P. S. J. Russell, "Raman-free, noble-gas-filled photonic-crystal fiber source for ultrafast, very bright twin-beam squeezed vacuum," Phys. Rev. Lett. **115**, 143602 (2015).
15. W. J. Wadsworth, N. Joly, J. C. Knight, T. A. Birks, F. Biancalana, and P. S. J. Russell, "Supercontinuum and four-wave mixing with q-switched pulses in endlessly single-mode photonic crystal fibres," Opt. Express **12**, 299–309 (2004).
16. K. Garay-Palmett, H. J. McGuinness, O. Cohen, J. S. Lundeen, R. Rangel-Rojo, A. B. U'ren, M. G. Raymer, C. J. McKinstrie, S. Radic, and I. A. Walmsley, "Photon pair-state preparation with tailored spectral properties by spontaneous four-wave mixing in photonic-crystal fiber," Opt. Express **15**, 14870–14886 (2007).
17. N. J. Cerf, M. Bourennane, A. Karlsson, and N. Gisin, "Security of quantum key distribution using d-level systems," Phys. Rev. Lett. **88**, 127902 (2002).
18. F. Benabid and P. Roberts, "Linear and nonlinear optical properties of hollow core photonic crystal fiber," J. Mod. Opt. **58**, 87–124 (2011).
19. P. S. J. Russell, P. Hölzer, W. Chang, A. Abdolvand, and J. Travers, "Hollow-core photonic crystal fibres for gas-based nonlinear optics," Nat. Photonics **8**, 278 (2014).
20. F. Couny, F. Benabid, P. Roberts, P. Light, and M. Raymer, "Generation and photonic guidance of multi-octave optical-frequency combs," Science **318**, 1118–1121 (2007).
21. N. Litchinitser, A. Abeeluck, C. Headley, and B. Eggleton, "Antiresonant reflecting photonic crystal optical waveguides," Opt. Lett. **27**, 1592–1594 (2002).

22. B. Debord, A. Amsanpally, M. Chafer, A. Baz, M. Maurel, J. Blondy, E. Hugonnot, F. Scol, L. Vincetti, F. Gérôme, and F. Benabid, "Ultralow transmission loss in inhibited-coupling guiding hollow fibers," Optica **4**, 209–217 (2017).

23. M. Zeisberger and M. A. Schmidt, "Analytic model for the complex effective index of the leaky modes of tube-type anti-resonant hollow core fibers," Sci. Rep. **7**, 11761 (2017).

24. M. Zeisberger, A. Hartung, and M. Schmidt, "Understanding dispersion of revolver-type anti-resonant hollow core fibers," Fibers **6**, 68 (2018).

25. B. Debord, M. Alharbi, T. Bradley, C. Fourcade-Dutin, Y. Wang, L. Vincetti, F. Gérôme, and F. Benabid, "Hypocycloid-shaped hollow-core photonic crystal fiber part i: Arc curvature effect on confinement loss," Opt. Express **21**, 28597–28608 (2013).

26. L. Vincetti, "Empirical formulas for calculating loss in hollow core tube lattice fibers," Opt. Express **24**, 10313–10325 (2016).

27. M. Liscidini and J. Sipe, "Stimulated emission tomography," Phys. Rev. Lett. **111**, 193602 (2013).

28. B. Fang, O. Cohen, M. Liscidini, J. E. Sipe, and V. O. Lorenz, "Fast and highly resolved capture of the joint spectral density of photon pairs," Optica **1**, 281–284 (2014).

29. K. Zielnicki, K. Garay-Palmett, D. Cruz-Delgado, H. Cruz-Ramirez, M. F. O'Boyle, B. Fang, V. O. Lorenz, A. B. U'Ren, and P. G. Kwiat, "Joint spectral characterization of photon-pair sources," J. Mod. Opt. **65**, 1141–1160 (2018).

30. A. Eckstein, G. Boucher, A. Lemaître, P. Filloux, I. Favero, G. Leo, J. E. Sipe, M. Liscidini, and S. Ducci, "High-resolution spectral characterization of two photon states via classical measurements," Laser Photonics Rev. **8**, L76–L80 (2014).

31. M. Azhar, G. Wong, W. Chang, N. Joly, and P. S. J. Russell, "Raman-free nonlinear optical effects in high pressure gas-filled hollow core pcf," Opt. Express **21**, 4405–4410 (2013).

32. K. Lynch-Klarup, E. Mondloch, M. Raymer, D. Arrestier, F. Gérôme, and F. Benabid, "Supercritical xenon-filled hollow-core photonic bandgap fiber," Opt. Express **21**, 13726–13732 (2013).

33. A. Hitachi, V. Chepel, M. I. Lopes, and V. N. Solovov, "New approach to the calculation of the refractive index of liquid and solid xenon," J. Chem. Phys. **123**, 234508 (2005).

34. A. Bideau-Mehu, Y. Guern, R. Abjean, and A. Johannin-Gilles, "Measurement of refractive indices of neon, argon, krypton and xenon in the 253.7–140.4 nm wavelength range. dispersion relations and estimated oscillator strengths of the resonance lines," J. Quant. Spectrosc. Radiat. Transf. **25**, 395–402 (1981).

35. M. Azhar, N. Joly, J. Travers, and P. S. J. Russell, "Nonlinear optics in xe-filled hollow-core pcf in high pressure and supercritical regimes," Appl. Phys. B **112**, 457–460 (2013).

36. M. Barbier, I. Zaquine, and P. Delaye, "Spontaneous four-wave mixing in liquid-core fibers: towards fibered raman-free correlated photon sources," New J. Phys. **17**, 053031 (2015).

37. J. E. Heebner, P. Chak, S. Pereira, J. E. Sipe, and R. W. Boyd, "Distributed and localized feedback in microresonator sequences for linear and nonlinear optics," J. Opt. Soc. Am. B **21**, 1818–1832 (2004).

38. J. Notaros, J. Mower, M. Heuck, C. Lupo, N. C. Harris, G. R. Steinbrecher, D. Bunandar, T. Baehr-Jones, M. Hochberg, S. Lloyd, and D. Englund, "Programmable dispersion on a photonic integrated circuit for classical and quantum applications," Opt. Express **25**, 21275–21285 (2017).